Observed Correlation Between Local Topography and Passive Neutron Measurements from the Dynamic Albedo of Neutrons (DAN) Instrument on the Mars Science Laboratory (MSL) Rover

Steven D. Dibb[1], Craig Hardgrove[2], Jack Lightholder[2,3], Lena Heffern[4], and Bent Ehresmann[5]

[1]Bay Area Environmental Research Institute, NASA Ames Research Center, Moffett Field, CA, USA
[2]School of Earth and Space Exploration, Arizona State University, Tempe, AZ, USA
[3]Jet Propulsion Laboratory, California Institute of Technology, Pasadena, CA, USA
[4]Laboratory for Atmospheric and Space Physics, University of Colorado, Boulder, CO, USA
[5]Southwest Research Institute, Boulder, CO, USA

Corresponding author: Steven Dibb (dibb@baeri.org)

Key Points:

- Three sections of the MSL rover traverse exhibit increased thermal neutron count rates correlated with increased average local relief.
- The magnitude of the increase in relative neutron count rates near topography is dependent upon the source and the nearby hydrogen content.
- Future measurements from missions with neutron instruments could use this sensitivity to measure hydration of nearby high relief features.

Abstract

The Dynamic Albedo of Neutrons (DAN) instrument on the Mars Science Laboratory Curiosity rover primarily measures neutrons that have undergone interactions with rocks and materials in the rover's local environment. As the rover ascends Aeolis Mons, it may encounter more extreme local topography (e.g., cliffs, gullies, canyons). We present three parts of the rover's traverse in which local topography, expressed as the average local relief relative to the rover, is moderately to strongly correlated with an increase in passive thermal neutron count rates. These increases in count rates are consistent with results from radiation transport models of the instrument's performance near simulated topographic features. Additional DAN measurements in areas of high average local relief (>0.25 meters) within five meters of the instrument could bolster this correlation. DAN's sensitivity to topography in its passive mode could be utilized as a new measurement capability and has implications for the operation of future landed missions carrying neutron spectrometers (e.g., VIPER, MoonRanger, Lunar-VISE).

1 Introduction

The Mars Science Laboratory (MSL) *Curiosity* rover is currently operating in Gale Crater, Mars with a suite of science instruments that includes the Dynamic Albedo of Neutrons (DAN) instrument (Grotzinger et al., 2012; Mitrofanov et al., 2012). The DAN instrument is used to measure the spatial variability and energy distribution of neutrons in the local environment (Jun et al., 2013; Litvak et al., 2008; Mitrofanov et al., 2012). These measurements of neutrons are used to constrain bulk geological properties of the near-surface (<~1 m depth), including the water-equivalent hydrogen (WEH), neutron absorption and scattering cross-sections, and stratigraphy (e.g., Czarnecki et al., 2020; Gabriel at al., 2018; Hardgrove et al., 2011; Mitrofanov et al., 2014; Tate et al., 2015).

The DAN instrument can operate in two modes. The first is an 'active' mode (henceforth referred to as 'DAN active'), which uses a pulse neutron generator (PNG) to emit 14.1 MeV neutrons into the surface. The second mode is passive (henceforth referred to as 'DAN passive') and measures neutrons generated by the rover's Multi-Mission Radioisotope Thermoelectric Generator (MMRTG) and secondary neutrons generated during the interaction of galactic cosmic rays (GCRs) with the martian surface and atmosphere (Jun et al., 2013; Mitrofanov et al., 2012). Neutrons measured in both active and passive mode are moderated to lower energies through nuclear interactions in the subsurface and may eventually be measured by DAN (Mitrofanov et al., 2012; Tate et al., 2015).

Neutron count rates measured by DAN are compared to simulated count rates from radiation transport models with varied geologic properties (e.g., composition and subsurface variability with depth) until a best-fit model is determined (e.g., Sanin et al., 2015; Tate et al., 2015). Typical models for the analysis of DAN data utilize the Monte Carlo N-Particle (MCNP) transport code developed by Los Alamo National Laboratory (Goorley et al., 2012). These models include idealized versions of the rover body, the DAN instrument, and the local environment. The local environment in these MCNP models is assumed to be a flat surface. This is a valid assumption for the overwhelming majority of the rover's traverse in Gale Crater (Section 2.2).

However, as the rover ascends the northern slope of Aeolis Mons from the floor of Gale Crater, it continues to encounter higher relief topography. To our knowledge, this study is the first to identify a correlation between topographic relief near the rover and changes in neutron count rates. Tate et al. (2018) explored how rover tip and tilt are correlated with a decrease in count rates and therefore may influence interpreted subsurface geochemistry from DAN passive. Mitrofanov et al. (2012) and Sanin et al. (2015) used MCNP simulations to constrain the sensing footprint for DAN active to a circular region approximately two meters in diameter centered between the rear rover wheels. However, these simulations assumed a planar surface with no topography. Further constraints on the sensing footprint of DAN in both active and passive modes when near topography are needed.

In a related study, Eke et al. (2015) demonstrated that a ~1% variation in neutron count rates measured from the Lunar Prospector Neutron Spectrometer over lunar polar craters could increase the interpreted water-equivalent hydrogen content from ~1% to ~4%. It is reasonable to infer that the effect of local topography on DAN's count rates may be larger because the topography is on the scale of the instrument's height above the martian surface (<~1 m). Furthermore, DAN is not the only radiation detector on MSL where measurements may be correlated with local topography: Guo et al. (2021) reported a 5±1% decrease in the dose rate measured in the Radiation Assessment Detector (RAD) instrument's high energy neutron detector when the rover was parked at the base of the Murray Buttes. Secondly, Ehresmann et al. (2021) reported a 7.5% decrease in neutral particle (high-energy neutrons and gamma rays) count rates measured at the Murray Buttes, attributed to an increase in shielding offered by the mass of the Buttes.

Finally, while DAN is currently the only roving neutron spectrometer used for planetary exploration, other missions are in development that will carry neutron detectors to the surfaces of airless planetary bodies (e.g., Carnegie Mellon University's MoonRanger, Lunar-VISE, and NASA's VIPER Mission) (Colaprete et al. 2019; Donaldson Hanna et al. 2023; Fisch et al. 2021). These missions will likely use a similar method to interpret neutron count rates and therefore may benefit from a better understanding of the influence of local topography on neutron count rates. Furthermore, because the DAN PNG has a limited lifetime (Mitrofanov et al., 2012), DAN passive data will eventually become the primary data product from the instrument. Accurately constraining the effect of non-geochemical factors on DAN passive count rates is therefore important to continue the accurate interpretation of subsurface geochemistry with DAN passive as the mission continues.

The purpose of this work is to examine the relationship between thermal (low energy) neutron count rates measured by DAN and average local relief. We report DAN passive thermal neutron measurements from three sections of the rover's traverse where an increase in thermal neutron count rate is correlated with increased average local relief within five meters of the rover. We report relative count rates from a series of MCNP models with increasingly higher relief around the rover that are consistent with the measured DAN results. We also vary the water-equivalent hydrogen (WEH) in the simulated regolith of these models to compare the effect of varying geochemistry with varying local relief.

2 Methods

2.1 MSL Radiation Instruments and Data Records

The DAN instrument consists of a pair of ^{3}He neutron detectors (manufactured by LND Inc., type 253146), a pulse neutron generator, and associated electronics located on the right and left rear sections of the rover (Mitrofanov et al., 2012). The two neutron detectors are sensitive to different energy regimes of neutrons: the first detector, called the Counter of Total Neutrons (CTN) measures neutrons with energy <~0.01 MeV (10 keV), while the second detector, called the Counter of Epithermal Neutrons (CETN) is wrapped in a 1 mm thick layer of cadmium which efficiently absorbs neutrons with energy <0.4 eV. Neutrons below this energy are absorbed by the cadmium, and neutrons counted by CETN are termed ‘epithermal’. The difference in count rates measured by the two detectors is taken as the ‘thermal’ neutron count rate (i.e., neutrons with energies <0.4 eV). The ^{3}He detectors are cylindrical, with a diameter of 5.1 cm, a total length of 6.5 cm, and a ~4 cm long active volume. The two detectors are oriented such that the central axis of the cylinders is parallel to the rover long axis and are filled with ^{3}He gas at a pressure of 3 atm (Mitrofanov et al., 2012). The epithermal neutron count rates measured by DAN passive are largely spatially and temporally invariant (see below for more details) while

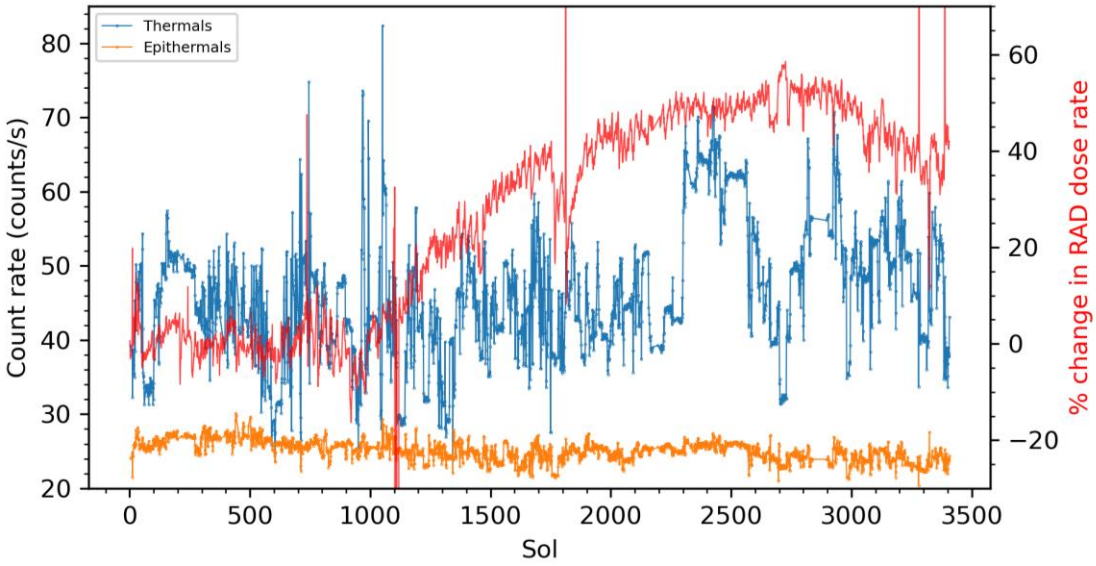

Figure 1. Thermal and epithermal neutron count rates measured by DAN passive for sols 3 through 3407. Thermal neutrons vary considerably throughout the mission (mean of 45.6 ± 9.3 counts/s 1σ) while epithermal neutrons (mean of 25.2 ± 1.9 counts/s 1σ) are less variable and have decreased steadily over the course of the mission, consistent with the decay of Pu in the rover’s MMRTG power source.The percent change in RAD dose rate relative to the mean of the dose rate over the first 1000 sols of the mission are shown in red. The RAD E (tissue-equivalent plastic scintillator) dose are mainly dominated by charged particle contributions. While the RAD E scintillator is capable of measuring neutrons the detection efficiency is much lower than for charged particles, and so only a subset of those neutrons prevalent on the Martian surface are recorded in the dose measurements.

the passive thermal neutron count rates are highly dependent on the local environment (Figure 1; Jun et al., 2013; Tate et al., 2015; Tate et al., 2018).

Reduced data records (RDRs) for the DAN instrument are publicly available on NASA's Planetary Data System Geosciences Node (https://pds-geosciences.wustl.edu/). A nominal DAN passive measurement in the RDRs contains (among other instrument telemetry) the number of counts measured in each detector in individual ~20-second time bins. A single RDR is composed of many of these time bins on a given Martian sol. In addition to the nominal measurements, these RDRs can contain other DAN time bins that contain counts measured during nominal but non-scientific activities, such as instrument warm-up or shutdown. In addition to the number of counts in each detector and the duration of a particular measurement bin, the RDRs contain the spacecraft clock (SCLK) value at the start of the measurement, the background count rate for each detector (see below for more discussion), and the latitude and longitude coordinates of each measurement. We removed measurements with off-nominal, non-science quality behavior (e.g., measurement durations ≠ 20 s, erroneous location data) and computed the count rate for each detector by dividing the counts of each measurement by the measurement length (in seconds) and then subtracting the background count rate.

The RAD instrument consists of a suite of six detectors: three silicon detectors (each 300 μm thick), a CsI scintillator, a plastic scintillator, and a further, surrounding plastic scintillator; RAD is described in detail in Hassler et al. (2012) and Zeitlin et al. (2016). The E detector dose rate (in μGy/day) recorded in the tissue-equivalent plastic scintillator is defined as a measure of the energy deposited above the threshold omnidirectionally (i.e., there are no coincidence requirements with other detectors). We present the dose rate measurements in detector E since it offers better statistics due to its much larger size (Ehresmann et al., 2021). Analysis of RAD E dose data was performed for this study using a notch filter to remove known diurnal variations in the data (Guo et al., 2018). The dose rate measurements from RAD sample the high-energy particle environment around the rover created primarily from bombardment by GCRs. Thus, RAD measurements can be used as a proxy for temporal variation in the flux of GCRs, which are one of the sources of thermal neutrons measured by DAN.

The DAN thermal and epithermal neutron count rates for sols 3-3407 are shown in Figure 1. Figure 1 also shows the percent change in the RAD E dose rate relative to the mean of the dose rate over the first 1000 sols of the mission. Analysis of the absolute dose rates from RAD near topography will be published in a forthcoming paper. Over the course of the mission, RAD has primarily seen variation in the dose rate corresponding to solar activity (e.g., solar cycle, energetic particle events, etc.), while the DAN thermal neutron count rates are more closely coupled to changes in the composition of rocks and soils around the rover.

Epithermal neutron count rates from DAN are significantly less variable than thermal neutron count rates and have decreased by ~9.9% over the course of the mission. As described by Jun et al. (2013), the rover's MMRTG is a constant source of epithermal neutrons with peak emission energies of ~3 MeV and maximum energies of ~10 MeV. The epithermal neutron population is replenished due to higher energy neutrons from the decay of Pu isotopes in the rover's MMRTG scattering down into the epithermal range. Simultaneously, epithermal neutrons are scattered down into the thermal range, keeping the total population of epithermal neutrons relatively constant. While the age and composition of the Pu fuel pellets in the rover's MMRTG are not known precisely, the decrease in epithermal count rates is roughly consistent with the mission duration as of sol 3407 (~10.125 years) and the half-life of ^{238}Pu (86.4 years), which Jun et al. (2013) assumed was >85% of the Pu mass in the MMRTG. It is important to note that many of these MMRTG-sourced neutrons interact with the rover body and are measured by DAN (Jun et al., 2013; Nikiforov et al., 2020; Sanin et al., 2015). It is estimated that the contribution to the DAN passive count rates from MMRTG-sourced neutrons scattered within the rover body back to the DAN detectors is 13.7 and 30.7 counts/second for the CETN and CTN detectors, respectively (Nikiforov et al., 2020; Sanin et al., 2015). Subtraction of these background count rates is included in our pipeline for retrieving DAN data from the PDS described above.

2.2 Topographic data for Curiosity's traverse

To compute local relief, we used the MSL Orbital DEM available in the MSL PLACES data volume on the PDS Imaging Node (https://pds-imaging.jpl.nasa.gov/). This DEM is constructed from MRO HiRISE and CTX images and MGS MOLA measurements (Calef et al., 2013). The DEM contains elevation measurements relative to a global areoid with a spatial resolution of 1.0 m/px (Calef et al., 2013). The absolute vertical accuracy of the DEM is tied to MOLA elevations (which have ~1 m absolute uncertainty) and its vertical precision is ≤0.2 m (Kirk et al., 2008; Smith et al., 2001).

Each of the DAN measurement bins in the RDRs has an associated latitude and longitude coordinate of the center of the rover frame of reference (i.e., on the nominal ground between the middle rover wheels) at the time the measurement was taken. We use these coordinates to create an 11x11 grid of DEM pixels centered on the pixel containing each DAN measurement (i.e., five meters in each direction). We computed the "average local relief" for each DAN measurement by computing the difference in elevation values (in meters) between each pixel and the central value of the grid and then computed the average of these differences. The vast majority (~98.6%) of DAN passive measurements were collected in areas where the absolute value of the local average relief was <0.25 m. Three sections of the traverse have significant average local relief (>0.25 m) with a substantial number of co-located DAN passive measurements. The sections are at locations named 'Hidden Valley' (sols 696-731), 'Mont Mercou' (sols 3049-3109), and the 'Maria Gordon Notch' (sols 3313-3329).

2.3 Utilization of Spearman's R

We use Spearman's rank correlation coefficient (henceforth called Spearman's R) to determine if there is a correlation between the DAN passive thermal neutron count rates and the average local relief. Spearman's R is a nonparametric measure of the rank correlation between two variable datasets and is useful for determining how well the relationship between those two variables can be described by a monotonic function (Kallner 2018). Like other correlation coefficients, values for Spearman's R range between -1 and +1. Positive values indicate the relationship between two variables can be described by a non-decreasing monotonic function (i.e., as variable 1 increases, variable 2 tends to increase). Negative values indicate the relationship can be described by a non-increasing monotonic function (i.e., as variable 1 increases, variable 2 tends to decrease). A Spearman's R near 0 indicates no significant correlation between the variables, and values closer to the extremes (-1 or +1) indicate a relationship closer to entirely non-decreasing (i.e., as variable 1 increases, variable 2 will never decrease) or entirely non-increasing (i.e., as variable 1 increases, variable 2 will never increase).

In this study, we compute Spearman's R using the DAN thermal neutron count rates described in Section 2.1 and the average local relief associated with each thermal neutron count rate measurement described in Section 2.2. For these datasets, a Spearman's R of 0 would indicate no relationship between the two. A Spearman's R of -1 would indicate that as average local relief increases, thermal neutron count rates always decrease. Alternatively, a Spearman's R of +1 would indicate that as average local relief increased, thermal neutron count rates always increased.

2.4 MCNP Modeling of DAN

Analysis of DAN data is performed through MCNP radiation transport models (e.g., Gabriel at al., 2018; Sanin et al., 2015; Tate et al., 2015). For this study, we used MCNP Version 6.1 (Goorley et al., 2012). We use a modified version of the models developed and described by Jun et al. (2013) and Mitrofanov et al. (2014). These models were developed during pre-flight calibration of the DAN instrument and the first several hundred sols of the MSL mission. Our model includes rover components (body, wheels, and DAN instrument) and the local environment, modeled as a ~120 m diameter sphere centered at the rear of the rover body (Figure 2). This sphere is split into two hemispheres of regolith and martian atmosphere.

We have modified the model of Jun et al. (2013) to include idealized cliff walls on either side of the rover, parallel to the long axis of the rover and DAN detectors (Figure 2). We varied the distance to and height of these walls to simulate the average local relief experienced by the rover and to quantify the relationship with the thermal neutron count rate. We modeled walls with heights of 0.25, 0.75, 1.0, and 2.5 m at distances of 1.0, 2.5, and 5.0 m, as well as a case with no walls. For each geometry, we simulated 10^7 particle histories in each MCNP simulation. An annotated schematic of a side and top view of one of the models is shown in Figure 2. Table 1 shows the wall height, distance, and equivalent average local relief of each simulation geometry. While the center point of our models is offset by ~1 m from the center of the 11x11 pixel grid described in Section 2.2, it does not affect the interpretation of our model results. This is because the walls in our models are symmetrical on either side of the rover and extend to the boundary of the 120 m sphere making up the full model space. Thus, the ~1 meter offset does not change the value of average local relief computed from the model geometry.

Table 1. Model geometries.

Wall Height (m)	Wall Distance (m)	Equivalent Average Local Relief (m)
0	0	0
0.25	2.5	0.11
0.25	1	0.18
0.75	2.5	0.34
1	2.5	0.45
0.75	1	0.55
1	1	0.73
2.5	2.5	1.14
2.5	1	1.82
5	2.5	2.27

We used the same composition for the underlying regolith and walls in all our simulations. This composition was taken from major oxides measured at the Sebina drill site (Jackson et al., 2018). Sebina represents a lacustrine mudstone composed of approximately 30% phyllosilicates, 25% feldspar, 20% Ca-sulfate, 15% hematite, 7% pyroxene, and 3% jarosite (Jackson et al., 2018). This geochemistry is consistent with compositions from

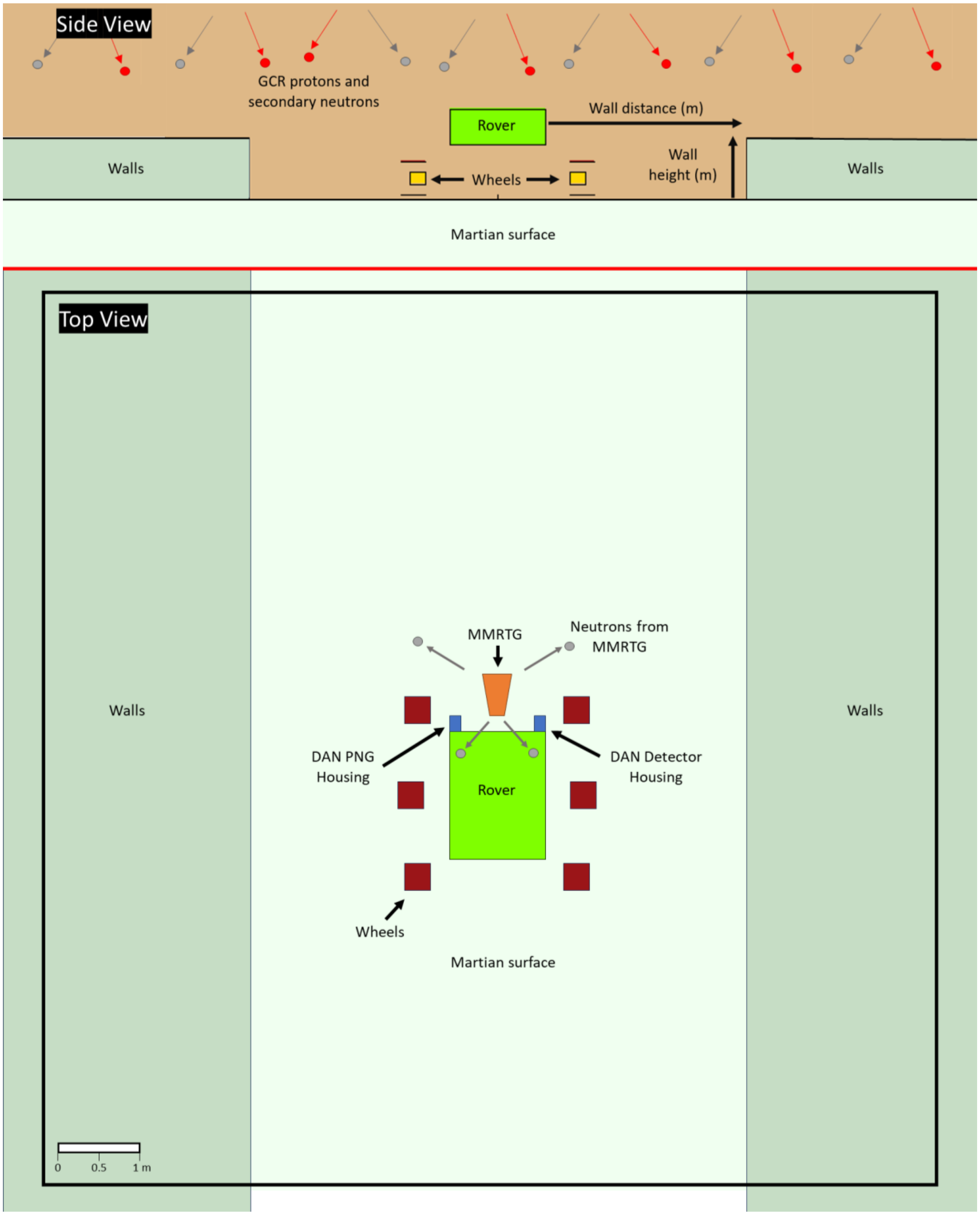

Figure 2. Side view and top view schematics of the MCNP models used in this study. The two views are separated by a red line. This model shows a 1 m high wall set 2.5 m from the rover body. In the side view, the GCR source is shown. In the top view, the MMRTG source location is shown. See text for discussion of sources. This cross-section shows only the central portion of the full model space, which is a sphere with a diameter of 120 m. In the top view, a black square shows the approximate size of the 11x11 m grid used to calculate average local relief.

253 the upper Murray Formation (Rampe et al., 2017) and represents an intermediate neutron

absorption cross section as determined from drill samples throughout the mission. To compare the effect of topography to changes in local hydration on thermal neutron count rates, we also varied the hydrogen in the model geochemistry. We report these abundances as water-equivalent hydrogen at 0.0, 1.5, 3.0, and 6.0 wt.% WEH, corresponding to 0, 1667, 3333, and 6666 ppm H, respectively. This range of WEH values was used because it spans the range of H abundances derived from DAN throughout the mission so far (Tate et al., 2018).

In our simulations, we use two separate source definitions. The first source is the GCR particle source developed by Jun et al. (2013) and Tate et al. (2015) for the analysis of DAN passive data. In our models, this source is modeled as a plane set 12 m above the ground and includes GCR protons and secondary spallation neutrons generated as the protons interact with the martian atmosphere. Tate et al. (2015, 2018) quantified the strength of the GCR source through a parameter termed $F_{GCR,RAD}$, which, as reported by Tate et al. (2018), has an average value over the first 753 sols of the mission of $3.53x10^7 \pm 3.64x10^6$ particles/s. The second source we use is the MMRTG source from Jun et al. (2013) developed for pre-flight calibration of DAN. As described by Jun et al. (2013), the age and composition of the MMRTG's Pu fuel are not precisely known, so quantifying its strength (i.e., activity) and emission spectrum after more than 10 years of operation is difficult. Using measurements taken during the assembly of the rover, Jun et al. (2013) reported the emission rate of the MMRTG was between $8.12x10^6$ and $1.00x10^7$ neutrons/s. It has likely weakened since then due to the steadily decreasing output of the MMRTG as evidenced by the decrease in epithermal neutron count rates measured by DAN (Figure 1). Assuming a 9.9% decrease in activity, it is reasonable to infer that the emission rate of the MMRTG is between ~$7.3\ x10^6$ and $9.0\ x10^6$ neutrons/s, or approximately 25% of the GCR source strength. We also note that the first 753 sols of the mission occurred during the peak of the last solar cycle. It has been shown that GCR flux in the inner solar system is anticorrelated with solar cycle, and therefore the GCR source strength computed by Tate et al. (2015, 2018) is likely significantly lower than the average for the entire mission (Dibb et al., 2023).

3 DAN and RAD Measurements

In this section, we show DAN thermal neutron count rates from three locations with significant average local relief. These locations are Hidden Valley (sols 696-731), Mont Mercou (sols 3049-3109), and the Maria Gordon Notch (sols 3313-3329). Additional narrative information about the rover team's activities and decisions can be found in Vasavada (2022).

In each of the map view figures (Figure 3A, 6A, and 9A), the count rates shown are the average thermal neutron count rate in a 50 cm pixel derived from the HiRISE orbital image mosaic of Gale Crater, which is shown as a grayscale image overlaying the color DEM in Figure 3A, 6A, and 9A. In these maps, north is up. The approximate location of the start of each sol on which there was a drive is indicated by the number of that sol. On those sols, the rover drove from that location to the next sol in chronological order. For example, on sol 696, the rover started driving on sol 696 from the location indicated '696' in Figure 3A to the location marked '702', where it remained parked until departing again on sol 702. Gaps in the plotted traverse paths indicate drives where no DAN passive data were collected. Points on the time series for each location (Figure 3B, 6B, and 9B) are colored using the same color ramp as the map view figures.

On each of the correlation plots (Figure 4, 7, and 10), we only show DAN data where the average local relief was greater than 0.1 m. This is done to examine the correlation in areas with potentially significant relief, as changes in the DAN count rates in areas of low average local relief (<0.1 m) are more correlated to the abundance of hydrogen and thermal neutron-absorbing elements in the subsurface.

Finally, for each location, we show the percent change in the rolling mean of the RAD dose rates (in µGy/day) to constrain the origin of any changes in the thermal neutron count rate. This percent change is relative to the mean of the rolling mean calculated for the sol range of interest.

3.1 Hidden Valley

On sols 696-705, the rover approached a partially dune-filled topographic low named Hidden Valley (Figure 3). Exposure of decimeter-scale bedding in the walls of Hidden Valley indicate the feature is composed of finely laminated mudstones which grade upward into thickly laminated facies, then back into thinly laminated facies, and finally into blocky, cross-bedded sandstone (Grotzinger et al., 2015). This interfingering transition between mudstone to sandstone is interpreted as the beginning of the stratigraphic contact between the Bradbury Group and the Murray Formation of the Mount Sharp Group (Bedford et al., 2020; Grotzinger et al., 2015). We note that the walls and floor of Hidden Valley both belong to the Bradbury Group, and that the formal contact between the units is ~10 meters up section and was not encountered until the Pahrump Hills on sol 753 (Bedford et al., 2020; Grotzinger et al., 2015). Thus, aside from the dune material at the center of Hidden Valley, it is unlikely that a significant difference in composition exists between the walls and floor material of the Hidden Valley feature.

DAN passive thermal neutron count rates from sols 696-731 are shown in map view and as a function of spacecraft clock time (SCLK) in Figures 3A and 3B. Figure 4 shows the relationship between average local relief and the thermal neutron count rate for DAN passive measurements with greater than 0.1 m average local relief during the Hidden Valley encounter.

The rover entered Hidden Valley on sol 706 and remained parked until sol 709, ~5 meters away from the north entrance wall (~1.5 m relief) and ~3.5 m away from the eastern entrance wall (0.5 m relief). DAN passive count rates increased from a mean count rate of 42.1 ± 3.16 counts/second on sols 703-705 (the “baseline” count rate, measured when the rover was ~15 m northeast, outside of Hidden Valley) to a mean of 64.2 ± 6.30 counts/second on sol 708 (the “first pass” measurement) (Figure 3B). Measured dose rates from RAD also decreased dramatically during this time (~4%, Figure 3B), consistent with other measurements from RAD near topographic features (Guo et al., 2021).

On sol 709, a reverse drive into the dune field of Hidden Valley was attempted and then aborted when excessive wheel slip was detected (Arvidson et al., 2017). During the sols the rover was on the dunes (sols 709-712), the DAN passive count rate dropped to an average of 28.9 ± 4.72 counts/second. This large drop in count rates is consistent with other measurements of neutrons from DAN while the rover is parked over sand: Gabriel et al. (2018) demonstrated that such basaltic sands are typically dehydrated (~<0.75 wt.% WEH) and therefore do not

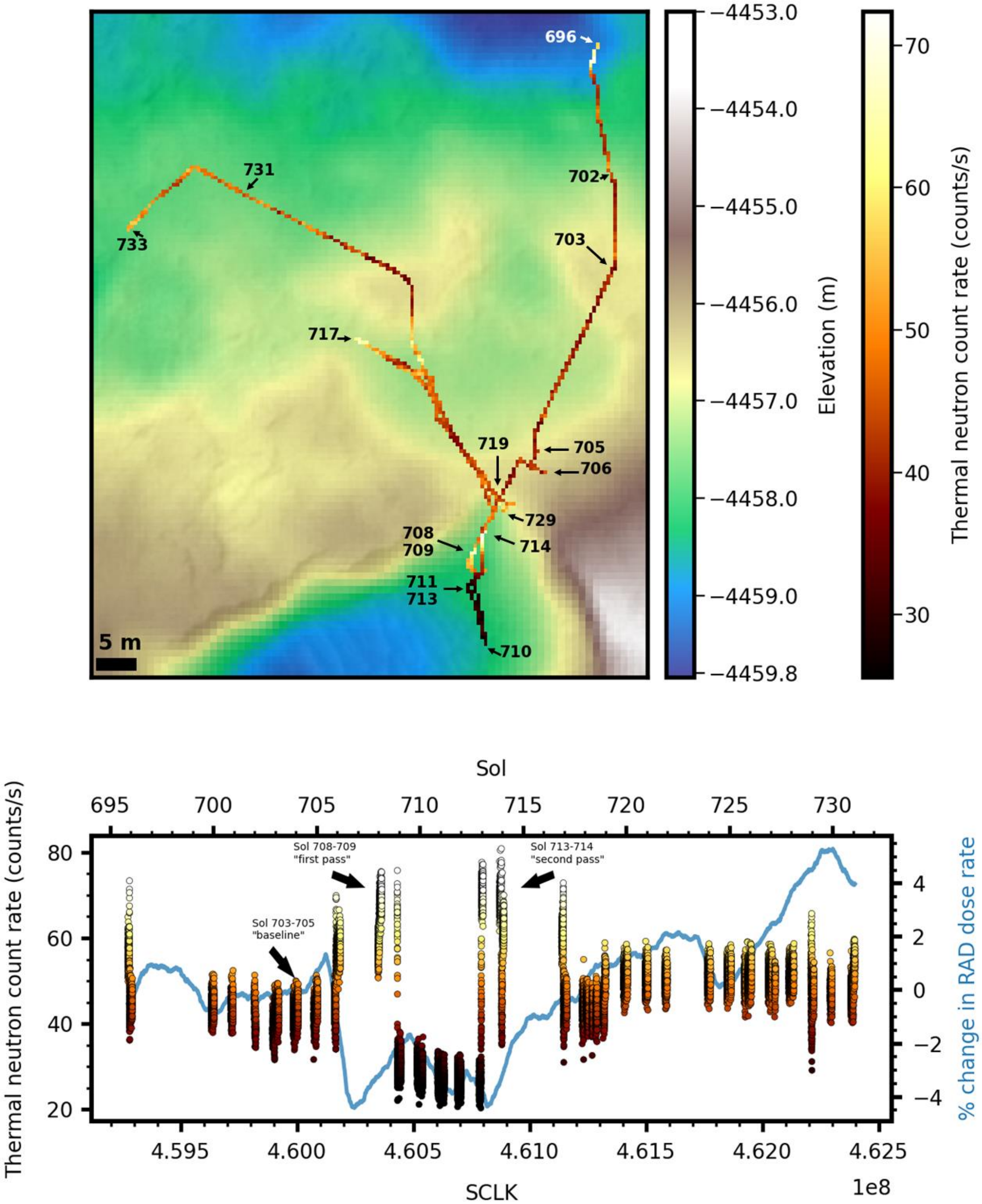

Figure 3. Map of the mean DAN thermal neutron count rates (A) and time series (B) during the Hidden Valley encounter (sols 696-731). The percent change in the RAD dose rate relative to the mean dose rate over sols 696-731 is shown as a blue line in (B). The approximate location of the start of each sol on which there was a drive is indicated.

effectively moderate neutrons, decreasing the observed thermal neutron counts (Gabriel et al., 2018).

Detailed study of possible drive paths suggested the safest route to exit Hidden Valley was the same way the rover had entered (Arvidson et al., 2017). The rover remained on the dune field until sol 713, when it drove north back towards the entrance to Hidden Valley. After the drive on sol 713, the DAN detectors were positioned ~4 m from the north wall and ~3 m from the ~0.5 m rise towards the southeast entrance wall, resulting in the highest average local relief seen during the Hidden Valley encounter (Figure 4). Here, the DAN passive count rate peaked at 70.0 ± 3.32 counts/second (the "second pass"), a ~65% increase from count rates measured on sols 703-705 when the rover was outside Hidden Valley and in flatter terrain. The rover remained parked at this location until late on sol 714, when it exited Hidden Valley and drove ~25 meters northwest (Figure 3A). RAD measured an increase in dose rate during the rover's exit from Hidden Valley, returning to dose rates similar to those measured before the rover entered Hidden Valley (Figure 3B).

The rover's departure from Hidden Valley was halted to attempt a new drilling technique at the transition between two sandstone units outcropping at the entrance to Hidden Valley (Abbey et al., 2020). Thus, the rover drove back toward the entrance of Hidden Valley on sol 717. The rover remained parked from sol 719 to sol 729 approximately 6 meters northeast of the location where DAN had previously measured elevated thermal neutron count rates. At this location, the rover was positioned on the ramp into Hidden Valley, with an average local relief of

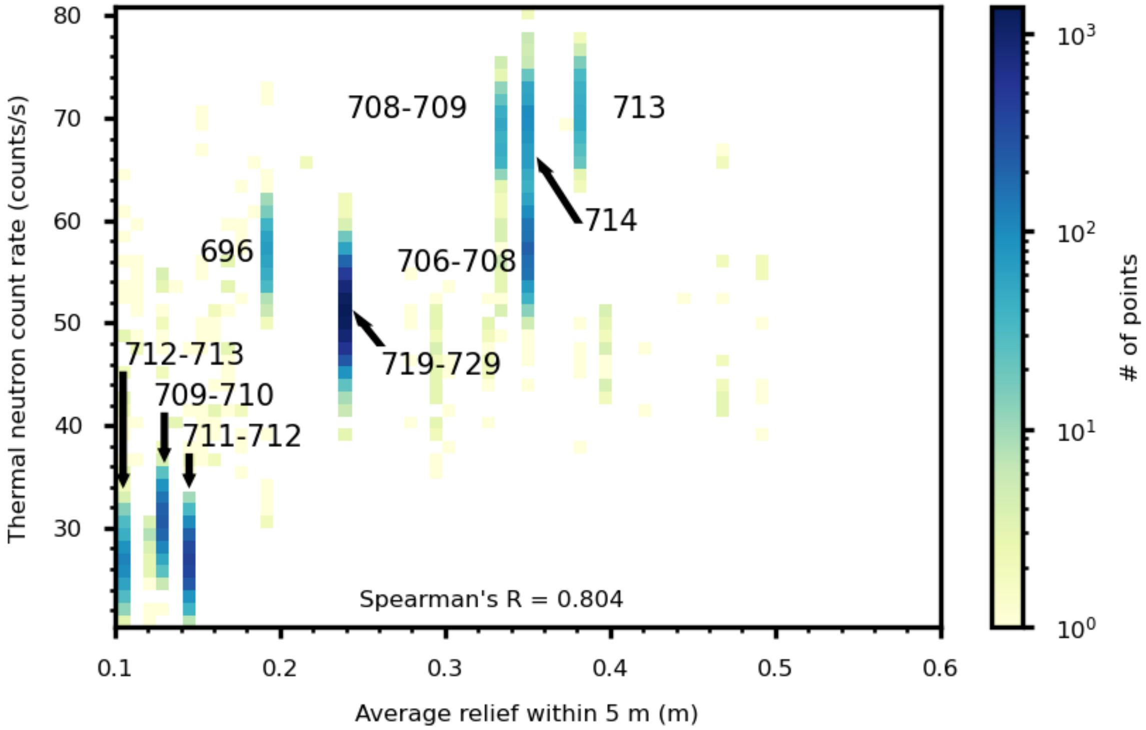

Figure 4. Average relief versus thermal neutron count rate for the Hidden Valley encounter (sols 696-731). Annotated sol ranges indicate when measurements during the Hidden Valley encounter were acquired. The Spearman's R value of 0.804 for this encounter suggests a strong positive monotonic correlation between local average relief and thermal neutron count rates.

~0.25 m. The mean thermal neutron count rate at this location was 50.9 ± 3.14 counts/second (Figure 3B). The rover departed the Hidden Valley area on sol 729.

3.2 Mont Mercou

On sol 3049, the rover began approaching the base of a ~6 m high, ~15 m wide cliff named Mont Mercou (Figure 5). This outcrop is in the southeastern part of the Glen Torridon region and lies within the transition between the clay-rich rocks of Glen Torridon and the more sulfate-rich unit further to the south (Bennett et al., 2022). While Mont Mercou represents some of the highest relief visited by the rover, the ground to the north of the outcrop features abundant sand (Figure 5). As described below, this sand strongly depressed the thermal neutron count

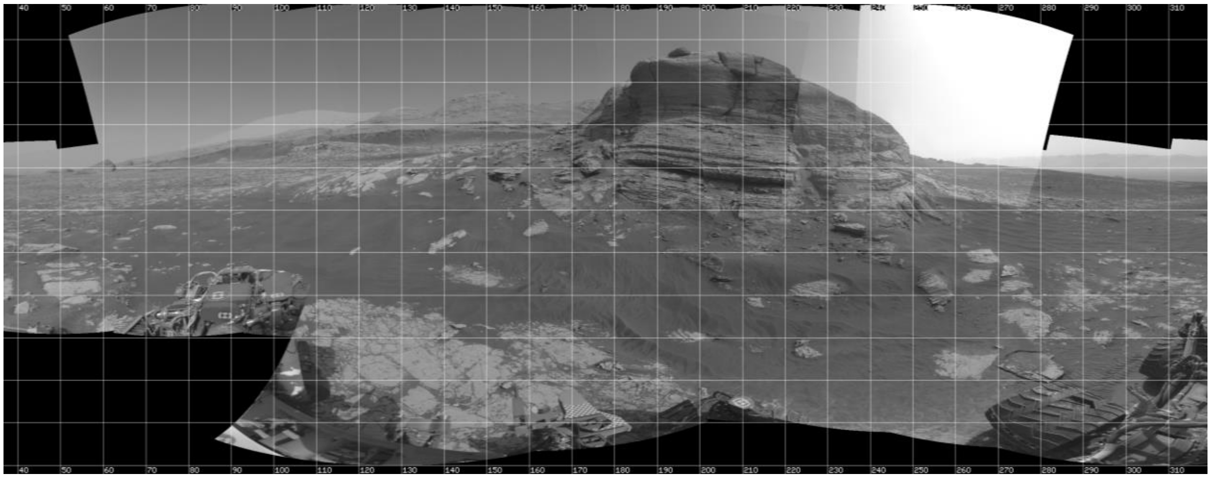

Figure 5. Mosaic of Navcam images (N_L000J3070XILT087CYL_S_0792_A0157M1_2PCT) of Mont Mercou, taken on sol 3070 at the location indicated ‘3072’ in Figure 6A. Heading and tilt angles are indicated by the white grid overlay. Dark-colored sand is present on much of the northern side of the Mont Mercou outcrop, over which the rover was parked during the close approach on sols 3072-3074.

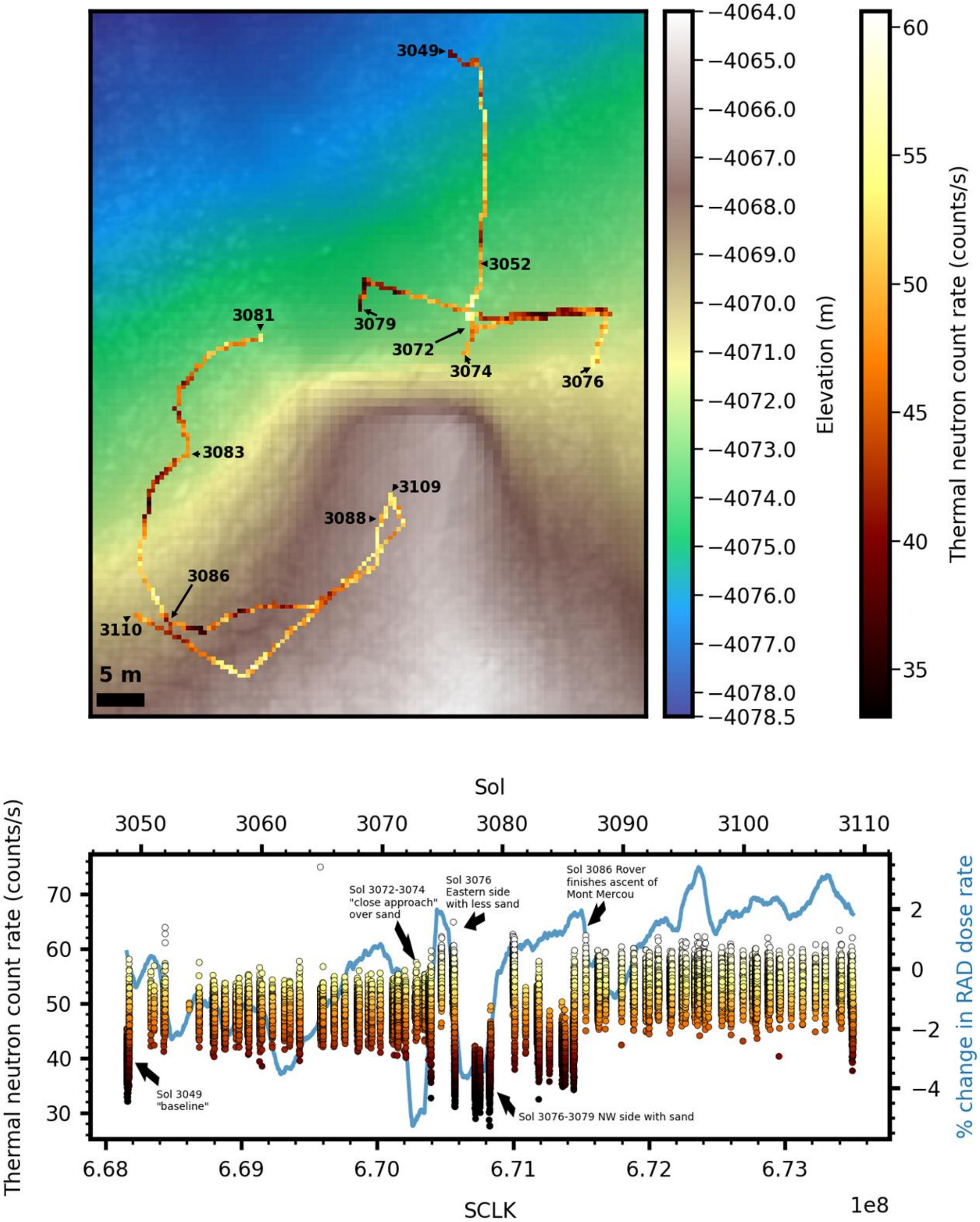

Figure 6. Map of the mean DAN thermal neutron count rates (A) and time series (B) during the Mont Mercou encounter (sols 3049-3110). The percent change in the RAD dose rate relative to the mean dose rate over sols 3049-3110 is shown as a blue line in (B). The approximate location of the start of each sol on which there was a drive is indicated. Gaps in the plotted traverse paths indicate drives where no DAN passive data were collected.

rates, as was seen at Hidden Valley and in other locations with high sand content (e.g., the Bagnold Dunes; Gabriel et al., 2018).

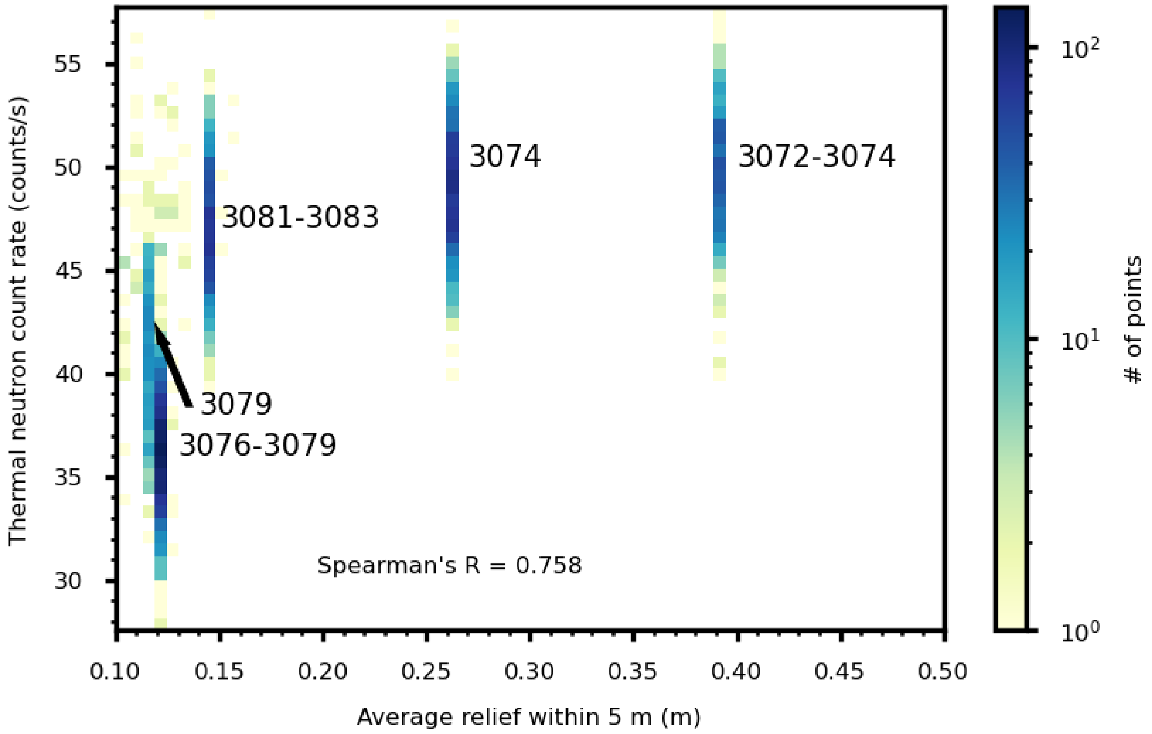

Figure 7. Average relief versus thermal neutron count rate for the Mont Mercou close approach encounter (sols 3070-3083). Annotated sol ranges indicate when measurements during the Mont Mercou encounter were acquired. The Spearman's R value for this location was 0.758, suggesting a positive monotonic correlation with approximately the same strength as that experienced at Hidden Valley.

DAN passive thermal neutron count rates from sols 3049-3110 are shown in map view and as a function of spacecraft clock time (SCLK) in Figure 6A and 6B. Figure 7 shows the relationship between average local relief and thermal neutron count rate for DAN passive measurements with greater than 0.1 m average local relief during the Mont Mercou encounter.

DAN measured a count rate of 39.3 ± 2.3 counts/second (the "baseline" measurement) before the drive on sol 3049, when the rover was approximately 30 m from the base of Mont Mercou (Figure 6A). After the drive on sol 3049, DAN measured a mean count rate of 49.4 ± 2.7 counts/second and remained parked until sol 3052. At this location (indicated by '3052' in Figure 6A), the rover was ~10 m from the base of the cliff.

On sol 3052, the rover drove south-southwest approximately 5 m towards Mont Mercou and remained parked at this new location until sol 3072 (Figure 6A). The count rate did not change significantly after this drive and remained relatively constant at 47.8 ± 2.7 counts/second (Figure 6B). The rover resumed driving on sol 3072, when it rotated nearly 180° and reversed, placing the rear of the rover ~2.5 m from the base of the cliff at the location indicated '3074' in Figure 6A. The thermal neutron count rate measured during this "close approach" measurement was 49.1 ± 2.3 counts/second, a ~25% increase relative to the "baseline" measurements from sol 3049, when the rover was on flatter ground.

While it appears that little of interest happened during the Mont Mercou close approach (sols 3072-3074), this is not entirely unexpected. It is well-documented that gas proportional counters like DAN are significantly less sensitive to neutrons incident end-on (i.e., those that enter the tube at low angles relative to the tube axis) than those that enter the tube perpendicular to the tube axis (e.g., Peplowski et al., 2020, Peplowski et al. 2023). Therefore, during the close approach to Mont Mercou described above, neutrons emitted from the cliff face may have gone undetected by the DAN detector tubes. Secondly, we note that the point of closest approach was in an area of high sand coverage (Figures 5 and 6A). DAN measurements from other areas of high sand coverage often exhibit a dramatic decrease in the thermal neutron count rate. Examples of such decreases in the count rate include the Hidden Valley dunes, subsequent drives at Mont Mercou across sand, and the Bagnold Dunes measurements reported by Gabriel et al. (2018). The lack of a more significant change in the thermal neutron count rate when the rover was parked at the closest approach to Mont Mercou suggests the expected decrease in count rate while over sand was compensated by the increase in count rate while near topography. Secondly, we note that on sol 3072, RAD measured a significant decrease in the dose rate (~5% µGy/day) (Figure 6B), consistent with expected decreases in dose rate near topography (Guo et al., 2021).

On sol 3074, the rover drove ~15 m northeast before rotating again to drive 5 m south. During the first part of this drive, the rover crossed one of the larger sand patches present at Mont Mercou. During this crossing, the thermal neutron count rate dropped below 40 counts/second (Figure 6). After the drive on sol 3074, the rover was positioned to the east of Mont Mercou and DAN measured a mean count rate of 54.6 ± 1.11 counts/second (the “Eastern side” annotation in Figure 6B). At this location (marked at ‘3076’ in Figure 6A), the rover was parked within 2.0 m of a 0.5 m rise and was over significantly less sand compared to the close approach of Mont Mercou. As expected, RAD measured an increase in dose rate contemporaneous with this drive away from Mont Mercou (Figure 6B).

On sol 3076, the rover began a series of drives that would loop around the northern side of Mont Mercou, steadily climbing a ramp on the western side of the feature (and thus decreasing the average local relief), and eventually place the rover on top of the outcrop. On sol 3076, the rover backtracked to the north and then rotated to drive ~30 m west. DAN again measured depressions in the thermal neutron count rate during the drives across the sandy areas (Figure 6). After the first drive, the rover parked at this new location (marked ‘3079’ in Figure 6A). At this location, the rover was ~7.5 m away from the feature and the average thermal neutron count rate was 36.1 ± 2.12 counts/second. Again, this drop in the thermal neutron count rate is consistent with previous measurements while parked over sand (this study and Gabriel et al. 2018). Dose rates from RAD were once again depressed (Figure 6B), as the rover had repositioned closer to Mont Mercou.

On sol 3079, the rover began the second drive of the series by rotating to drive approximately 10 m west-southwest before parking ~7 m from the cliff (Figure 6A). At this position (marked ‘3081’ in Figure 6A), the rover was positioned over more exposed rock and the thermal neutron count rate increased to 52.6 ± 0.86 counts/second (Figure 6B). The rover remained parked at this position until sol 3081, when it drove ~10 m to the south-southwest up the ramp on the western side of Mont Mercou. At this new location (marked ‘3083’ in Figure 6A), the thermal neutron count rate dropped to a mean of 47.1 ± 2.57 counts/second (Figure 6B). The rover continued ascending this ramp on sol 3083 and parked at the location marked ‘3086’ on Figure 6A, where the mean count rate was 44.1 ± 2.38 counts/second. These steady decreases in thermal neutron count rate as the rover drove up the ramp on the western side of Mont Mercou are consistent with our hypothesis that decreased average local relief produces a relative decrease in thermal neutron count rate.

The rover resumed driving on sol 3086 with the intent of capturing a drill sample from the top of the sequence of rocks that form Mont Mercou. At its new position on the top of the outcrop (marked ‘3088’ in Figure 6A), the mean thermal neutron count rate measured by DAN was 52.8 ± 2.64 counts/second (Figure 6B). After collecting remote sensing observations, the rover drove ~4 meters north-northeast on sol 3088 to continue to search for a drill site. The rover remained parked at this location (marked ‘3109’ in Figure 6A) until sol 3109, where the mean count rate measured by DAN was 53.3 ± 2.53 counts/second (Figure 6B). The rover collected its 31st drill sample on sol 3094 and continued to collect follow up remote sensing measurements from the high vantage point until 3109 (Vasavada 2022). On sol 3109, the rover drove ~45 m southwest. At this location (marked ‘3110’ in Figure 6A), the rover was ~3 m from the location it parked after driving on sol 3083 and measured a similar count rate of 46.5 ± 2.40

counts/second (Figure 6B). This location represents the final stop of the Mont Mercou campaign (Vasavada 2022).

3.3 Maria Gordon Notch

Our final study location is the Maria Gordon Notch, which the rover passed through on sols 3319-3329. The Maria Gordon Notch is a narrow pass between cliff-forming outcrops on the eastern flank of the Greenheugh Pediment (Figures 9A and 9B). The walls of the Maria Gordon Notch are slope-forming formations of the Mount Sharp group capped by erosion-resistant layers of the Stimson formation (Banham et al., 2022). Geochemical analyses of float rocks derived from the capping unit on sol 3324 indicate that they are compositionally similar to other outcrops of the Stimson formation (Banham et al., 2022). Several dedicated DAN measurements were

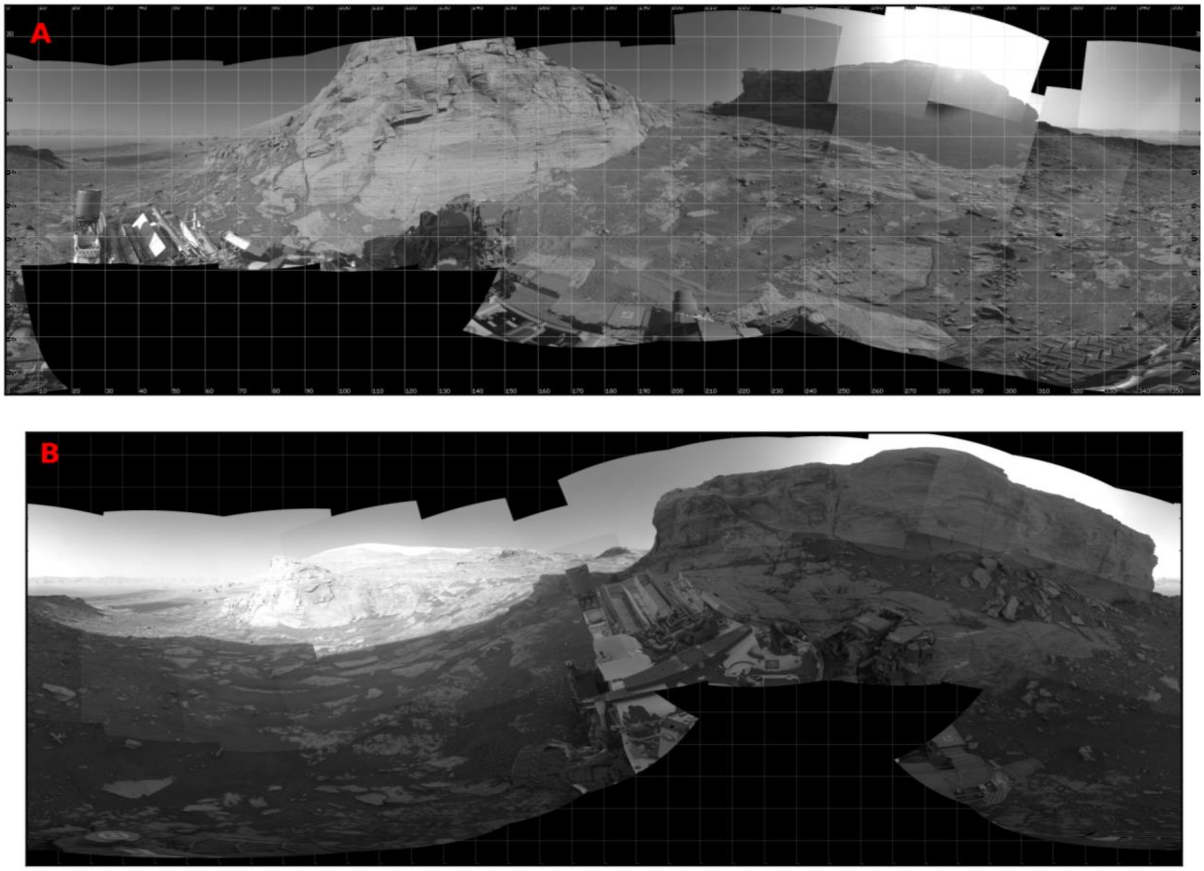

Figure 8. Navcam mosaics taken during the Maria Gordon Notch encounter. (a) Mosaic of Navcam images (N_L000J3322XILT091CYL_S_3204_P1106M1_2PCT) taken at the location indicated ‘3322’ in Figure 9A. (b) Mosaic of Navcam images (N_R000_3324_ILT092CYL_S_0084_UNCORM1_2PCT) taken at the location indicated ‘3324’ in Figure 9A. The center of both images is pointed approximately south. Heading and tilt angles are indicated by the white grid overlay. Dark-colored sand is present throughout much of the Maria Gordon Notch but is particularly present along the western wall (lower left corner of (b)), where the rover was positioned on sol 3326. Both mosaics here have been brightened by an additional 70% to highlight shadowed areas.

organized during this encounter to explore the influence of topography on both DAN active and passive data.

The rover deviated from a nominal southward path through the Notch on sol 3318 to investigate boulders that had fallen from the rock unit capping the Notch (Figure 9A). The mean thermal neutron count rate measured by DAN passive at this location (marked '3318' in Figure 9A) was 39.6 ± 2.47 counts/second (Figure 9B). On sol 3318, the rover drove ~45 m southeast and then south towards the narrower section of the Notch, stopping ~15 m north of it (marked '3319' in Figure 9A). At this stop, DAN measured an average thermal neutron count rate of 39.0 ± 2.25 counts/second (indicated as the "baseline" count rate in Figure 9B). This area north of the Notch has relatively low relief (<~0.2 m, Figure 10).

On sol 3319, the rover began its approach towards the eastern wall of the Maria Gordon Notch, parking ~4 m from the base of the sloping eastern wall. Here, DAN measured an average thermal neutron count rate of 53.8 ± 2.51 counts/second ("Eastern Wall" Figure 9B), an increase of ~35% when compared to measurements acquired further north, away from the eastern wall. RAD measured a decrease in the dose rate (~10% µGy/day) during this approach. The rover remained parked at this location (marked '3322' in Figure 9A) until sol 3322 when it drove south, subparallel to the eastern wall before turning to drive across the notch and reach the

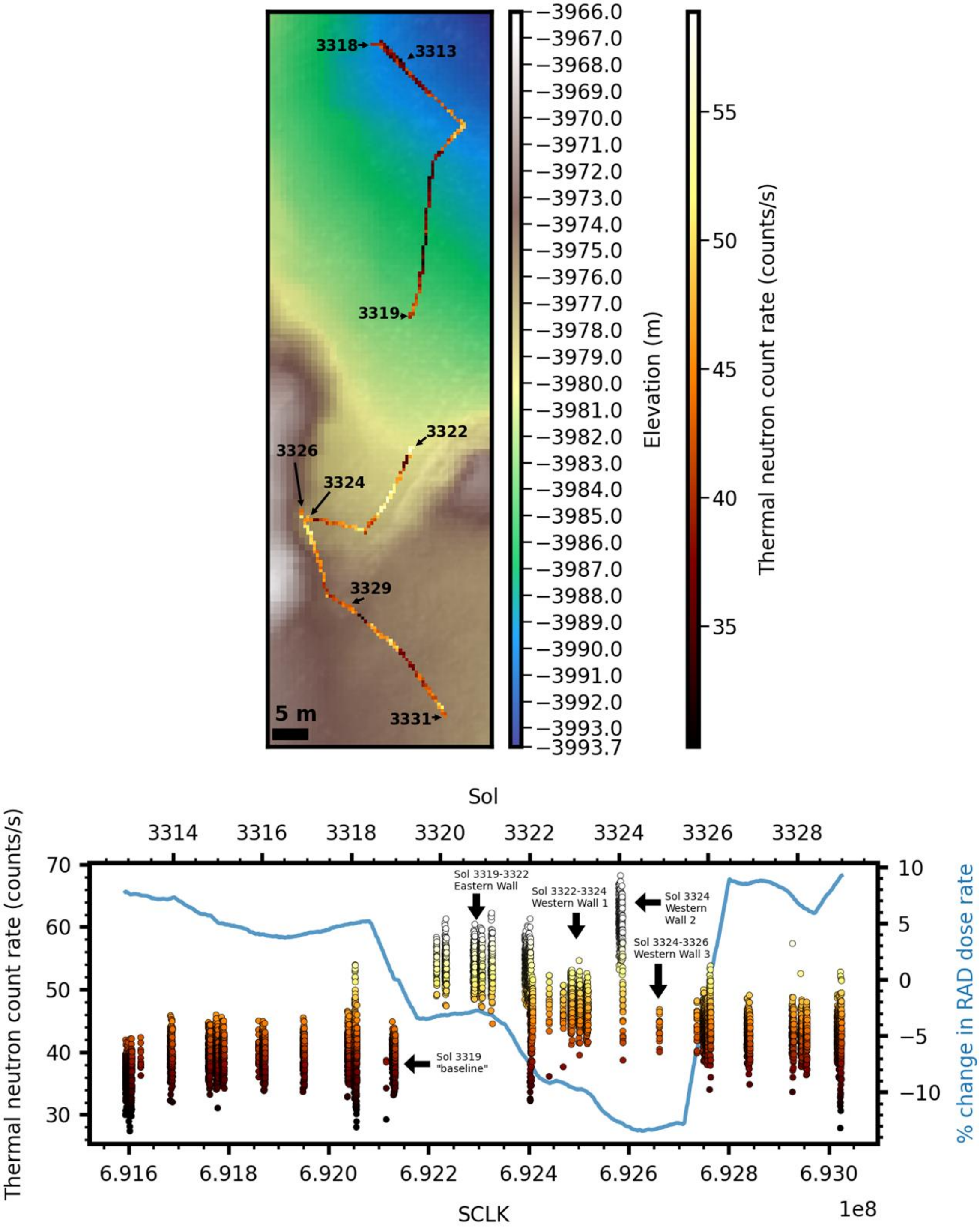

Figure 9. Map of the mean DAN thermal neutron count rates (A) and time series (B) during the Maria Gordon Notch encounter (sols 3313-3329). The percent change in the RAD dose rate relative to the mean dose rate over sols 3313-3329 is shown as a blue line in (B). The approximate location of the start of each sol on which there was a drive is indicated. Gaps in the plotted traverse paths indicate drives where no DAN passive data were collected.

western wall. At this new location ~5 m from the western wall (marked '3324' in Figure 9A), the mean count rate measured by DAN was 47.2 ± 2.50 counts/second ("Western Wall 1" in Figure

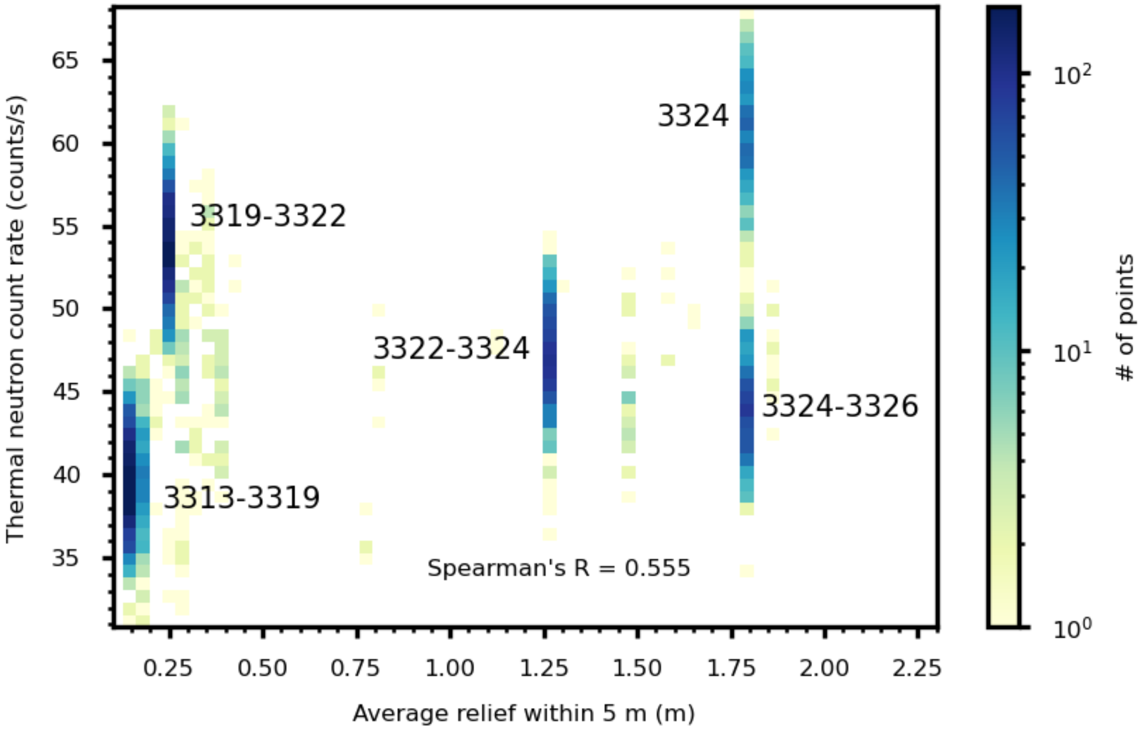

Figure 10. Average relief versus thermal neutron count rate for the Maria Gordon Notch encounter (sols 3313-3329). The Spearman's R value for this location was 0.555, suggesting a positive monotonic correlation.

9B). During this time, RAD measured a further decrease in the dose rate (Figure 9B). On sol 3324, the rover rotated and reversed, placing the rear of the rover close to the base of the western wall. During this operation, the mean count rate measured by DAN increased to 60.1 ± 3.60 counts/second ("Western Wall 2" in Figure 9B).

Late on sol 3324, the rover rotated back to approximately parallel with the western wall and drove ~2 m north-northwest. At this final location at the base of the western wall (marked '3326' in Figure 9A), the mean count rate dropped to 43.3 ± 2.88 counts/second ("Western Wall 3" in Figure 9B). The sand coverage at this location is higher than at the eastern wall or at the first location on sol 3324 (Figure 8). After performing contact science on sol 3326, the rover reversed out of the notch to the south, parking at the southern end of the feature (marked '3329' in Figure 9A). Here, the mean thermal neutron count rate was 42.5 ± 2.31 counts/second, and the measured RAD dose rate rose dramatically to values similar to those recorded before the rover entered the Maria Gordon Notch (Figure 9B). Finally, the rover exited the Maria Gordon Notch area on sol 3329.

4 Discussion

At each of the three locations presented here, we observe increases in the thermal neutron count rate measured by DAN that are significantly correlated with increases in average local relief. A summary of some of the results at each location is shown in Table 2, which contains the measured increase in thermal neutron count rate at each of the locations, the corresponding value for average local relief, and the Spearman's R between average local relief and thermal neutron

Table 2. Summary of thermal neutron count rate changes at each of the locations in this study.

Location	**Sol(s)**	**Count Rate (counts/s)**	**% Change From Baseline**	**Average Local Relief (m)**	**Spearman's R**
Hidden Valley					
Baseline	703-705	42.1 ± 3.16	--	<0.1	0.804
First Pass	706-709	64.2 ± 6.30	$\mathbf{52^{+29}_{-24}}$ %	0.35	
Second Pass	713-714	70.0 ± 3.32	$\mathbf{66^{+22}_{-19}}$ %	0.38	
Mont Mercou					
Baseline	3049	39.3 ± 2.3	--	<0.1	0.758
Close approach	3072-3074	49.1 ± 2.3	$\mathbf{25^{+14}_{-12}}$ %	0.39	
Maria Gordon Notch					
Baseline	3318-3319	39.0 ± 2.25	--	<0.1	0.555
Eastern Wall	3319-3322	53.8 ± 2.51	$\mathbf{38^{+15}_{-14}}$ %	0.26	
Western Wall 1	3322-3324	47.2 ± 2.50	$\mathbf{21^{+14}_{-13}}$ %	1.26	
Western Wall 2	3324	60.1 ± 3.60	$\mathbf{54^{+19}_{-17}}$ %	1.75	
Western Wall 3	3324-3326	43.3 ± 2.88	$\mathbf{11^{+15}_{-13}}$ %	1.75	

count rates for that location. Table 2 also shows the percent change from a nearby "baseline" DAN measurement (i.e., a measurement taken in a nearby area of low average local relief). This percent change was calculated by dividing the specific measurement by the baseline measurement. The range of values of the percent change in Table 2 reflect the minimum and maximum possible differences in thermal neutron count rates for that measurement, using the uncertainty on the count rates listed in Table 2.

Finally, at each of the three study locations, our results are consistent with Gabriel et al. (2018), who showed that basaltic sands in Gale Crater are dehydrated and exhibit a strongly decreased thermal neutron count rate. It is an unfortunate reality that sand is often co-located with topography, likely because topography offers breaks in prevailing winds that deposit sand.

4.1 Implications From MCNP Models

To better understand the influence that local topography is having on thermal neutron count rates measured by DAN, we used MCNP to simulate relative changes in count rates for a variety of topographic cases and subsurface hydrogen content using both the GCR and MMRTG source definitions described in Section 2.4 and in more detail by Jun et al. (2013) and Tate et al. (2015, 2018). Figure 11 shows the relative change in thermal neutron flux (in neutrons/cm^2/s/source particle) for the different values of average local relief and wt.% water-equivalent hydrogen (WEH) used in our models. Figure 11A shows the results using the GCR source and Figure 11B shows the results using the MMRTG source. Figure 11C shows the ratio between the model results from the two sources. All results in Figure 11 are normalized to the model with 0 meters of average local relief and 0.0 wt.% WEH. It is important to note that the model results presented in Figures 11A and 11B are *per source particle* and an absolute interpretation of the model results depends on an accurate understanding of the strength of each source. Because the neutron output from the MMRTG source is not publicly available, we discuss these results in their relative terms.

Figures 11A and 11B indicate that increasing WEH in cases with no walls (i.e., average local relief of 0 m) increases the thermal neutron count rate measured by DAN contributed from both sources. This is consistent with previous studies of DAN data (e.g., Gabriel et al. 2018; Tate et al. 2018) and studies of neutrons on other airless planetary bodies (e.g., Eke et al. 2015). In this case, the increase in hydrogen in the subsurface acts to thermalize more neutrons. We note that the change in count rate is greater for MMRTG-sourced neutrons than for GCR-sourced neutrons, likely because many of the neutrons emitted by the MMRTG are in the epithermal energy range, which are particularly sensitive to increasing hydrogen (Hardgrove et al. 2011; Jun et al., 2013; Mitrofanov et al. 2012).

Second, increasing average local relief increases the thermal neutron count rate for neutrons sourced from both the MMRTG and GCRs. For dry regolith (i.e., 0 wt.% WEH), the increase in count rate is comparable for a neutron produced from either GCRs or the MMRTG. This is evidenced by the comparable slopes of best-fit lines to the model cases with 0 wt.% WEH (black points in Figures 11A and 11B). With increasing hydration, however, the relative increase in thermal neutron count rate from MMRTG-sourced neutrons is greater than the relative increase in count rate from GCR-sourced neutrons. In the extreme case, our models indicate that there will be ~25x as many MMRTG-sourced neutrons detected by DAN if the rover were to approach topographic features like those in our models with an average local relief of 2.27 m (equivalent to 5 m high walls 2.5 m away from the rover) and 6 wt.% WEH, compared to a dry regolith (0 wt.% WEH) and no topography. In contrast, our models indicate that there will be only a ~6x increase in the number of GCR-sourced neutrons in the same comparison. Again, this is likely due to the greater sensitivity of epithermal neutrons from the MMRTG to increasing hydration. Because there has never been a 25-fold increase in the count rate, we can infer from our models that DAN is measuring a mixture of GCR and MMRTG-sourced neutrons in relatively dry, flat terrain.

The Spearman R values for each set of models at a constant WEH are shown in Figures 11A and 11B. Our models indicate very strong positive monotonic relationships between the average local relief and the modeled thermal neutron flux for both sources. We note that the correlation coefficients are much stronger than any of the coefficients from our study areas, which is interpreted as an indication that local relief is not the only variable changing between the real DAN passive measurements. In reality, deviations from the ideal topography of our models and variations in geochemistry and sand coverage under the rover are continually convoluting any signal from variation in local relief.

Variation in the flux of galactic cosmic rays is another important influence on neutron count rates measured by DAN, however, the dose rate measurements from RAD at each of our study locations indicate that GCR flux variation was not the primary driver of neutron count rate variation. In fact, consistent with Guo et al. (2021), we note that RAD typically measured a decrease in the dose rate in the locations described in this study, where DAN measured an increase in the thermal neutron count rate. Furthermore, our results are consistent with the lack of observed correlation between RAD data and DAN thermal neutron count rates for the entire rover traverse (as seen in Figure 1 and reported by Martinez-Sierra et al. (2019)) because of the opposite effects on the two datasets when the rover is near topography. Finally, our results imply that the low energy neutron flux ($E < 0.4$ eV) around topography increases and therefore represents a concern for future human missions to Mars and habitat placement.

Figures 11A and 11B also show a first-degree polynomial fit to each set of model results at constant WEH. We use a general definition of the coefficient of determination (R^2) to evaluate the goodness of fit for each of these polynomials. These fits imply that at a constant WEH, increasing average relief produces an approximately linear increase in the modeled relative thermal neutron flux. The slopes of these lines and their relative offset from the dry (i.e., 0 wt.% WEH) and flat model can be used to generate updated estimates of WEH from DAN passive.

For example, during the Hidden Valley encounter, DAN measured a thermal neutron count rate of 32.5 ± 3.32 counts/second when the rover was positioned on the eastern edge of the dune field (at the location marked ‘710’ in Figure 3A). In contrast, DAN measured a count rate of 64.2 ± 6.30 counts/second at the northern entrance wall (at the location marked ‘708/709’ in Figure 3A). This factor of ~2.0 ± 0.28 increase in the count rate is shown as a horizontal band in Figures 11A and 11B. Tate et al. (2018) interpreted this change in count rate as an increase from 0.2 ± 0.1 wt.% WEH to 4.2 ± 0.4 wt.% WEH. When considering only GCR-sourced neutrons (Figure 11A), our models are consistent with this interpretation for a flat geometry (i.e., zero local relief), but are also consistent with a more modest increase in the local hydrogen abundance (e.g., 1.5 wt.% WEH) in combination with the increased average local relief observed at Hidden Valley (~0.35 m, Figure 4). Alternatively, when considering just MMRTG-sourced neutrons (Figure 11B), our models are consistent with no change in hydration in Hidden Valley. Instead, our models suggest that the increase in count rates seen at Hidden Valley may have solely been caused by the increase in average local relief.

Figure 11C shows the ratio between the relative change in thermal neutron count rate from MMRTG and GCR-sourced neutrons. The ratio stays roughly constant at a particular WEH as a function of average local relief. For example, the ratio between the change in thermal neutron count rate from MMRTG-sourced neutrons and GCR-sourced neutrons is ~1 when in dry conditions (0 wt.% WEH), regardless of the change in average local relief. In a more hydrated environment, the ratio is ~6, indicating that MMRTG-sourced neutrons are more likely to contribute to the measured DAN count rate than GCR-sourced neutrons. However, as noted in Section 2.4, the strength of the MMRTG (in neutrons/s) is possibly less than a third of the GCR source strength computed by Tate et al. (2015, 2018) over the first 753 sols of the mission. Due to the lack of definitive compositional information on the MMRTG fuel, it is extremely difficult to determine which of these two sources are the dominant contributor to the increase in neutron count rate near topography.

There is one final important interpretation from Figure 11. The slopes of the polynomial fits in Figure 11A and 11B increase with increasing hydrogen content. This implies that hydrogen abundance of both the ground beneath the rover and the topographic feature itself could be constrained by collecting a series of neutron measurements at increasing proximity to the topography. The slope of a line connecting these measurements as a function of average local relief could be used to quantify the hydrogen abundance of the topography. Deviation from a

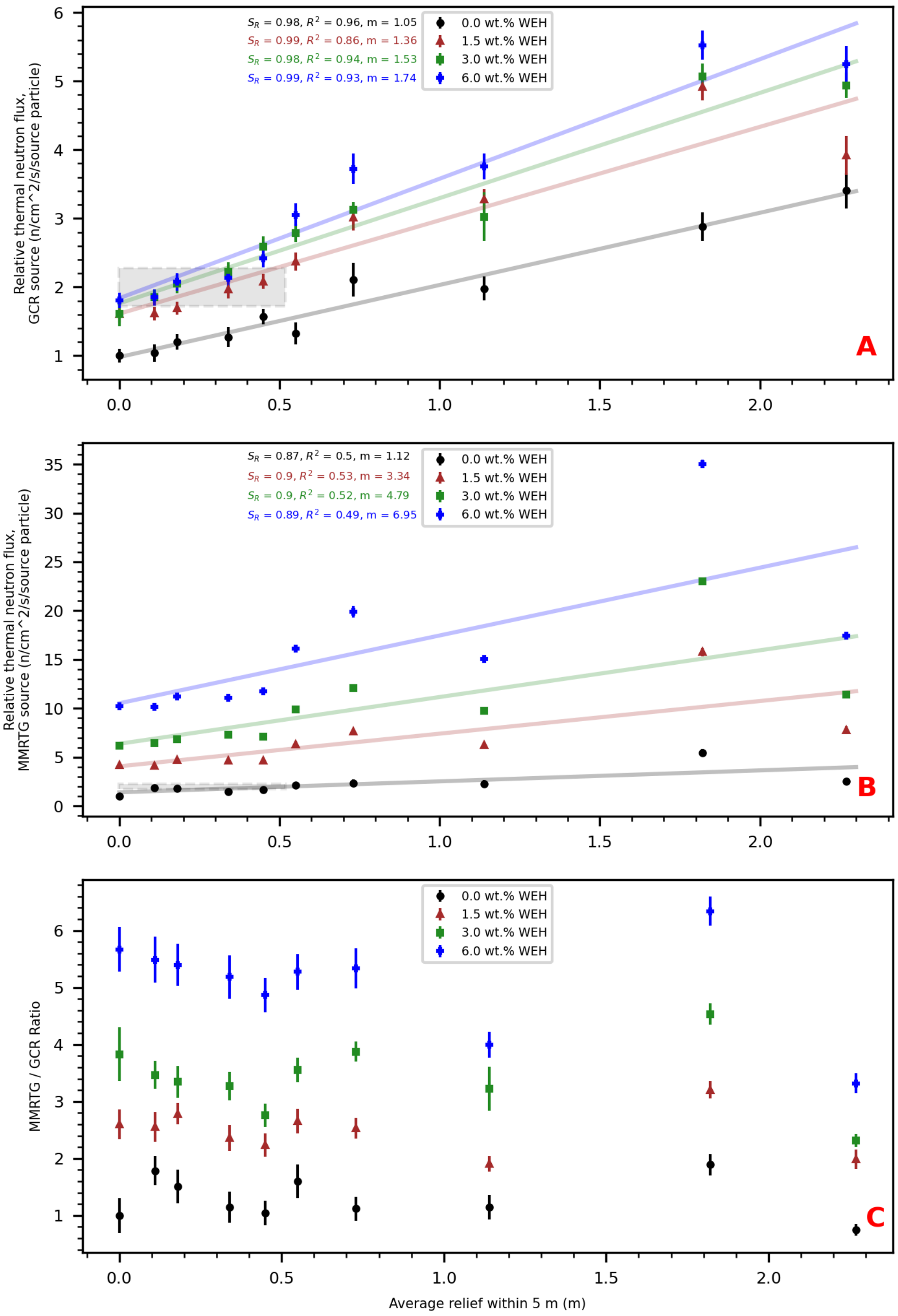

Figure 11. Average relief versus relative thermal neutron flux from our MCNP models using a (A) GCR and (B) MMRTG source from Jun et al. (2013) and Tate et al. (2015). Variations in the hydrogen abundance in the models (reported as wt.% WEH) are shown as different colors and symbols. The Spearman R values, coefficients of determination (R^2), and slopes (m) of linear fits to the model sets at each value of WEH are shown in A and B. Upper and lower bounds of the gray box in A and B indicate the variation in count rate observered at Hidden Valley (sols 696-731), while left and right bounds indicate the range of average local relief experienced at Hidden Valley. (C) The ratio between the results in A and B, indicating that the relative contributions from both sources are roughly constant at a particular WEH regardless of change in average local relief.

linear fit implies a difference in the hydrogen abundance between the topographic feature and the underlying terrain if the compositions of the two units are otherwise similar.

We conclude that local topographic relief can, and does, influence the low energy neutron environment, and therefore, the thermal neutron count rates measured by DAN. Our models indicate that, for both MMRTG and GCR-sourced neutrons, increasing average local relief is consistent with an increase in the thermal neutron count rate. This is likely due to an increase in bulk density and macroscopic neutron scattering cross-section in the volume of space around the rover caused by the presence of topography. The increase in these two properties likely moderates more neutrons to lower energies and scatters them onto trajectories more detectable by DAN. Future measurements with DAN or future surface missions with similar nuclear instrumentation (e.g., Carnegie Mellon University's MoonRanger, Lunar-VISE , and NASA's VIPER Mission) could leverage this sensitivity to interpret the hydration of cliff-forming units, boulders, or other outcrops by measuring a difference in thermal neutron count rate from the expected increase from higher local relief (Colaprete et al. 2019; Donaldson Hanna et al. 2023; Fisch et al. 2021).

5 Conclusions

We have documented three locations from the MSL rover's traverse with a moderate to strong correlation between average local relief and thermal neutron count rate measured by DAN. While the hydration and composition of the material within the DAN sensing area most strongly influences the low energy (thermal) neutron count rates, we find that local topography can cause significant increases in the measured thermal neutron count rate from DAN and can even counteract the decrease in count rate caused by sand coverage.

To understand the correlation between thermal neutron count rate and topography, we have simulated the effect of local topography on the DAN instrument using Monte Carlo radiation transport models. Our simulations are consistent with an increase in the passive thermal neutron count rate measured by DAN with increased average local relief. This increase is larger for models with higher hydrogen abundance. Neutrons emitted by the MMRTG are relatively more likely to contribute to the increase in thermal neutron count rates than GCR-sourced neutrons with increasing average local relief and hydration. However, the lack of detailed information on the composition and age of the MMRTG fuel makes more absolute determination of which source is contributing to the measured count rate extremely difficult. Future measurements with DAN and RAD could focus on constraining the relative strengths of these two sources.

Looking to the future, the sensitivity of passive neutron data to local topography may offer new measurement capabilities as the rover continues to ascend Aeolis Mons. In general, this work demonstrates the importance of including nearby slopes and topographic features in the reduction and interpretation of passive surface neutron data. While the DAN instrument on the MSL rover is currently the only active roving neutron spectrometer on a planetary mission, future missions to the Moon and other planets should, when appropriate, include topography in their analyses to more accurately constrain local hydration and to potentially study the hydration of nearby topographic features (within <5 meters of the instrument).

Acknowledgments

We are grateful to T.S.J. Gabriel, S. Czarnecki, I. Jun, L. M. Martínez Sierra, and the RAD Team for thoughtful discussions about DAN, MCNP, and RAD. This work used archived data in NASA's Planetary Data System and we express our gratitude to the Geosciences Node at Washington University in St. Louis and the Imaging Node at the Jet Propulsion Laboratory. S. Dibb, C. Hardgrove, and J. Lightholder were supported under NASA MSL Participating Scientist Grant 80NSSC22K0770. L. Heffern and B. Ehresmann are part of the RAD Team and are supported by NASA SMD/Heliophysics and HEOMD/AES under JPL subcontract #1273039 to SwRI and by DLR in Germany under contract with Christian-Albrechts-Universitat (CAU).

Data Availability

Reduced Data Records from the DAN instrument are publicly available on NASA's Planetary Data System at https://pds-geosciences.wustl.edu/msl/msl-m-dan-3_4-rdr-v1/. Map data for the Mars Science Laboratory mission are available at https://pds-imaging.jpl.nasa.gov/data/msl/MSLPLC_1XXX/. The MCNP files used in this study contain export-controlled information and will not be made publicly available but may be made available upon request by contacting the lead author. Requesters must demonstrate their access to the MCNP code by attaching the email approval from the Oak Ridge National Laboratory Radiation Safety Information Computing Center (RSICC) in their correspondence. After registration with RSICC, the MCNP code is obtained using the "Submit Request" function at https://rsicc.ornl.gov/CustomerService.aspx. Full instructions for obtaining the MCNP code are found at https://mcnp.lanl.gov/how_to_get_the_mcnp_code.html, tips for using it are found at https://mcnp.discourse.group/login, and information on formal classes can be found at https://mcnp.lanl.gov/classes.html.

References

1. Abbey, W., Anderson, R., Beegle, L.W., Peters, G., Morookian, J.M., Biesiadecki, J., Carsten, J., Collins, C., Davis, K., Kinnett, R. and Klein, D., 2020. A look back, part II: The drilling campaign of the Curiosity rover during the Mars Science Laboratory's second and third martian years. Icarus, 350, p.113885.

2. Arvidson, R.E., Iagnemma, K.D., Maimone, M., Fraeman, A.A., Zhou, F., Heverly, M.C., Bellutta, P., Rubin, D., Stein, N.T., Grotzinger, J.P. and Vasavada, A.R., 2017. Mars science laboratory curiosity rover megaripple crossings up to sol 710 in gale crater. Journal of Field Robotics, 34(3), pp.495-518.

3. Banham, S., Bedford, C., Gupta, S., Roberts, A., Dietrich, W., Bryk, A., Rubin, D., Grotzinger, J., Weintraub, A., House, C. and Caravaca, G., 2022, March. Correlation of Aeolian Stratigraphy Across the Greenheugh Pediment, Gale Crater: Yeah, It's More Stimson Formation. LPSC 50, Abstract #2363.

4. Bedford, C.C., Schwenzer, S.P., Bridges, J.C., Banham, S., Wiens, R.C., Gasnault, O., Rampe, E.B., Frydenvang, J. and Gasda, P.J., 2020. Geochemical variation in the

Stimson formation of Gale crater: Provenance, mineral sorting, and a comparison with modern Martian dunes. Icarus, 341, p.113622.

5. Bennett, K.A., Fox, V.K., Bryk, A., Dietrich, W., Fedo, C., Edgar, L., Thorpe, M.T., Williams, A.J., Wong, G.M., Dehouck, E. and McAdam, A., 2022. The Curiosity Rover's Exploration of Glen Torridon, Gale crater, Mars: An Overview of the Campaign and Scientific Results. Journal of Geophysical Research: Planets, p.e2022JE007185.

6. Calef, F.J., Dietrich, B., Edgar, L., Farmer, J., Fraeman, A., Grotzinger, J., Palucis, M., Parker, T., Rice, M., Rowland, S.K. and Stack, K.M., 2013, March. Geologic mapping of the Mars Science Laboratory landing ellipse. LPSC 44, Abstract #1719.

7. Colaprete, A., Andrews, D., Bluethmann, W., Elphic, R.C., Bussey, B., Trimble, J., Zacny, K. and Captain, J.E., 2019, December. An overview of the Volatiles Investigating Polar Exploration Rover (VIPER) mission. In AGU Fall Meeting Abstracts (Vol. 2019, pp. P34B-03).

8. Czarnecki, S., Hardgrove, C., Gasda, P.J., Gabriel, T.S.J., Starr, M., Rice, M.S., Frydenvang, J., Wiens, R.C., Rapin, W., Nikiforov, S. and Lisov, D., 2020. Identification and description of a silicic volcaniclastic layer in Gale crater, Mars, using active neutron interrogation. Journal of Geophysical Research: Planets, 125(3), p.e2019JE006180.

9. Dibb, S.D., Elphic, R.C., Lawrence, D.J. and Peplowski, P.N., 2023. Estimates of Solar Modulation Potential to Support Lunar Exploration and Volatiles Prospecting with the Neutron Spectrometer System. LPI Contributions, 2806, p.2416.

10. Donaldson Hanna, K., Benavente, J., Bennett, K., Denevi, B., Dove, A., Hagerty, J., Hardgrove, C., Hayne, P., LaMee, A., Landis, M., Osterman, D., Prettyman, T., Shirley, K. A., Siegler, M., Sunshine, J., Williams, J-P., Valencia, S., Ball Aerospace team, and Arizona State University team, 2023. Lunar-VISE: An investigation of the Moon's non-mare silicic volcanism. LPSC 54, Abstract #2806.

11. Eke, V.R., Bower, K.E., Diserens, S., Ryder, M., Yeomans, P.E.L., Teodoro, L.F.A., Elphic, R.C., Feldman, W.C., Hermalyn, B., Lavelle, C.M. and Lawrence, D.J., 2015. The effect of craters on the lunar neutron flux. Journal of Geophysical Research: Planets, 120(8), pp.1377-1395.

12. Ehresmann, B., Hassler, D.M., Zeitlin, C., Guo, J., Wimmer-Schweingruber, R.F., Khaksari, S. and Loeffler, S., 2021. Natural radiation shielding on Mars measured with the MSL/RAD instrument. Journal of Geophysical Research: Planets, 126(8), p.e2021JE006851.

13. Fisch, P.R.M., Schweitzer, L.C., Jones, H.L. and Whittaker, W.L., 2021, March. Lunar Polar Autonomous Micro-Roving for Hydrogenous Volatile Characterization. LPSC 52, Abstract #2548.

14. Gabriel, T.S.J., Hardgrove, C., Czarnecki, S., Rampe, E.B., Rapin, W., Achilles, C.N., Sullivan, D., Nowicki, S., Thompson, L., Litvak, M. and Mitrofanov, I., 2018. Water

abundance of dunes in Gale Crater, Mars from active neutron experiments and implications for amorphous phases. Geophysical Research Letters, 45(23), pp.12-766.

15. Goorley, T., James, M., Booth, T., Brown, F., Bull, J., Cox, L.J., Durkee, J., Elson, J., Fensin, M., Forster, R.A. and Hendricks, J., 2012. Initial MCNP6 release overview. Nuclear Technology, 180(3), pp.298-315.

16. Grotzinger, J.P., Crisp, J., Vasavada, A.R., Anderson, R.C., Baker, C.J., Barry, R., Blake, D.F., Conrad, P., Edgett, K.S., Ferdowski, B. and Gellert, R., 2012. Mars Science Laboratory mission and science investigation. Space science reviews, 170(1), pp.5-56.

17. Grotzinger, J.P., Gupta, S., Malin, M.C., Rubin, D.M., Schieber, J., Siebach, K., Sumner, D.Y., Stack, K.M., Vasavada, A.R., Arvidson, R.E. and Calef III, F., 2015. Deposition, exhumation, and paleoclimate of an ancient lake deposit, Gale crater, Mars. Science, 350(6257), p.aac7575.

18. Guo, J., Lillis, R., Wimmer-Schweingruber, R.F., Zeitlin, C., Simonson, P., Rahmati, A., Posner, A., Papaioannou, A., Lundt, N., Lee, C.O. and Larson, D., 2018. Measurements of Forbush decreases at Mars: both by MSL on ground and by MAVEN in orbit. Astronomy & Astrophysics, 611, p.A79.

19. Guo, J., Khaksarighiri, S., Wimmer-Schweingruber, R.F., Hassler, D.M., Ehresmann, B., Zeitlin, C., Löffler, S., Matthiä, D., Berger, T., Reitz, G. and Calef, F., 2021. Directionality of the Martian surface radiation and derivation of the upward albedo radiation. Geophysical Research Letters, 48(15), p.e2021GL093912.

20. Hardgrove, C., Moersch, J. and Drake, D., 2011. Effects of geochemical composition on neutron die-away measurements: Implications for Mars Science Laboratory's Dynamic Albedo of Neutrons experiment. Nuclear Instruments and Methods in Physics Research Section A: Accelerators, Spectrometers, Detectors and Associated Equipment, 659(1), pp.442-455.

21. Hassler, D.M., Zeitlin, C., Wimmer-Schweingruber, R.F., Böttcher, S., Martin, C., Andrews, J., Böhm, E., Brinza, D.E., Bullock, M.A., Burmeister, S. and Ehresmann, B., 2012. The radiation assessment detector (RAD) investigation. Space science reviews, 170, pp.503-558.

22. Jackson, R.S., Wiens, R.C., Beegle, L.W., Rampe, E.B., Johnson, J.R., Forni, O. and Newsom, H.E., 2018. ChemCam Investigation of the Last Four MSL Drill Sites in the Murray Formation, Gale Crater, Mars.

23. Jun, I., Mitrofanov, I., Litvak, M.L., Sanin, A.B., Kim, W., Behar, A., Boynton, W.V., DeFlores, L., Fedosov, F., Golovin, D. and Hardgrove, C., 2013. Neutron background environment measured by the Mars Science Laboratory's Dynamic Albedo of Neutrons

instrument during the first 100 sols. Journal of Geophysical Research: Planets, 118(11), pp.2400-2412.

24. Kallner, A., 2018. Formulas. Laboratory statistics, pp.1-140.

25. Kirk, R.L., Howington-Kraus, E., Rosiek, M.R., Anderson, J.A., Archinal, B.A., Becker, K.J., Cook, D.A., Galuszka, D.M., Geissler, P.E., Hare, T.M. and Holmberg, I.M., 2008. Ultrahigh resolution topographic mapping of Mars with MRO HiRISE stereo images: Meter-scale slopes of candidate Phoenix landing sites. Journal of Geophysical Research: Planets, 113(E3).

26. Litvak, M. L., et al., 2008. "The dynamic albedo of neutrons (DAN) experiment for NASA's 2009 Mars science laboratory." Astrobiology 8.3: 605-612.

27. Martinez Sierra, L. M., Jun, I., Ehresmann, B., Hassler, D., Litvak, M. L., Martin, A. C., Zeitlin, C., 2019. Galactic Cosmic Ray Induced Neutron Environment at the Surface of Mars as Seen by MSL DAN Instrument. LPSC 50, Abstract #2923.

28. Mitrofanov, I.G., Litvak, M.L., Varenikov, A.B., Barmakov, Y.N., Behar, A., Bobrovnitsky, Y.I., Bogolubov, E.P., Boynton, W.V., Harshman, K., Kan, E. and Kozyrev, A.S., 2012. Dynamic Albedo of Neutrons (DAN) experiment onboard NASA’s Mars Science Laboratory. Space Science Reviews, 170(1), pp.559-582.

29. Mitrofanov, I.G., Litvak, M.L., Sanin, A.B., Starr, R.D., Lisov, D.I., Kuzmin, R.O., Behar, A., Boynton, W.V., Hardgrove, C., Harshman, K. and Jun, I., 2014. Water and chlorine content in the Martian soil along the first 1900 m of the Curiosity rover traverse as estimated by the DAN instrument. Journal of Geophysical Research: Planets, 119(7), pp.1579-1596.

30. Nikiforov, S.Y., Mitrofanov, I.G., Litvak, M.L., Lisov, D.I., Djachkova, M.V., Jun, I., Tate, C.G. and Sanin, A.B., 2020. Assessment of water content in martian subsurface along the traverse of the Curiosity rover based on passive measurements of the DAN instrument. Icarus, 346, p.113818.

31. Peplowski, P.N., Yokley, Z.W., Liebel, M., Cheng, S., Elphic, R.C., Hoogerheide, S.F., Lawrence, D.J. and Nico, J.S., 2020. Position-dependent neutron detection efficiency loss in 3He gas proportional counters. Nuclear Instruments and Methods in Physics Research Section A: Accelerators, Spectrometers, Detectors and Associated Equipment, 982, p.164574.

32. Peplowski, P.N., Elphic, R.C., Fritzler, E.L. and Wilson, J.T., 2023. Calibration of NASA’s Neutron Spectrometer System (NSS) for landed measurements of hydrogen content of the lunar subsurface. Nuclear Instruments and Methods in Physics Research Section A: Accelerators, Spectrometers, Detectors and Associated Equipment, 1049, p.168063.

33. Rampe, E.B., Ming, D.W., Grotzinger, J.P., Morris, R.V., Blake, D.F., Vaniman, D.T., Bristow, T.F., Morrison, S.M., Yen, A.S., Chipera, S.J. and Downs, R.T., 2017. Mineral

trends in early Hesperian lacustrine mudstone at Gale crater, Mars. LPSC 48, Abstract #2821.

34. Sanin, A.B., Mitrofanov, I.G., Litvak, M.L., Lisov, D.I., Starr, R., Boynton, W., Behar, A., DeFlores, L., Fedosov, F., Golovin, D. and Hardgrove, C., 2015. Data processing of the active neutron experiment DAN for a Martian regolith investigation. Nuclear Instruments and Methods in Physics Research Section A: Accelerators, Spectrometers, Detectors and Associated Equipment, 789, pp.114-127.

35. Smith, D.E., Zuber, M.T., Frey, H.V., Garvin, J.B., Head, J.W., Muhleman, D.O., Pettengill, G.H., Phillips, R.J., Solomon, S.C., Zwally, H.J. and Banerdt, W.B., 2001. Mars Orbiter Laser Altimeter: Experiment summary after the first year of global mapping of Mars. Journal of Geophysical Research: Planets, 106(E10), pp.23689-23722.

36. Tate, C.G., Moersch, J., Jun, I., Ming, D.W., Mitrofanov, I., Litvak, M., Behar, A., Boynton, W.V., Deflores, L., Drake, D. and Ehresmann, B., 2015. Water equivalent hydrogen estimates from the first 200 sols of Curiosity's traverse (Bradbury Landing to Yellowknife Bay): Results from the Dynamic Albedo of Neutrons (DAN) passive mode experiment. Icarus, 262, pp.102-123.

37. Tate, C.G., Moersch, J., Mitrofanov, I., Litvak, M., Bellutta, P., Boynton, W.V., Drake, D., Ehresmann, B., Fedosov, F., Golovin, D. and Hardgrove, C., 2018. Results from the dynamic albedo of neutrons (DAN) passive mode experiment: Yellowknife Bay to Amargosa Valley (Sols 201–753). Icarus, 299, pp.513-537.

38. Vasavada, A.R., 2022. Mission Overview and Scientific Contributions from the Mars Science Laboratory Curiosity Rover After Eight Years of Surface Operations. Space science reviews, 218(3), pp.1-65.

39. Zeitlin, C., Hassler, D.M., Wimmer-Schweingruber, R.F., Ehresmann, B., Appel, J., Berger, T., Böhm, E., Böttcher, S., Brinza, D.E., Burmeister, S. and Guo, J., 2016. Calibration and characterization of the Radiation Assessment Detector (RAD) on Curiosity. Space Science Reviews, 201, pp.201-233.